Geometry-dependent penetration fields of superconducting $Bi_2Sr_2CaCu_2O_{8+\delta}$ platelets

P. J. Curran,[1] J. R. Clem,[2] S. J. Bending,[1] Y. Tsuchiya[3] and T. Tamegai[3]
[1]Department of Physics, University of Bath, Claverton Down, Bath BA2 7AY, United Kingdom
[2]Ames Laboratory and Department of Physics and Astronomy, Iowa State University, Ames, Iowa, 50011-3160, USA
[3]Department of Applied Physics, The University of Tokyo, Hongo, Bunkyo-ku, Tokyo 113-8656, Japan

Magneto-optical imaging has been used to study vortex penetration into regular polygon-shaped $Bi_2Sr_2CaCu_2O_{8+\delta}$ platelets with various geometries (disks, pentagons, squares, and triangles) but known fixed areas. In all cases we observe an exponential dependence of the field of first penetration, H_p, on temperature, consistent with a dominant Bean-Livingston barrier for pancake vortices at our measurement temperatures (45 K – 80 K). However, the penetration field consistently decreases with decreasing degree of sample symmetry, in stark contrast to conventional estimates of demagnetization factors using equivalent ellipsoids based on *inscribed* circles, which predict the reverse trend. Surprisingly, this observation does not appear to have been reported in the literature before. We demonstrate empirically that estimates using equivalent ellipsoids based on *circumscribed* circles predict the correct qualitative experimental trend in H_p. Our work has important implications for the estimation of appropriate effective demagnetization factors for flux penetration into arbitrarily shaped superconducting bodies.

PACS number(s): 74.72.Gh, 74.25.Ha, 74.25.Op, 74.78.Na

I. INTRODUCTION

The Meissner phase in type-II superconductors is separated from the mixed state by the lower critical field, H_{c1}. Above H_{c1} the presence of flux in the form of quantized vortices becomes energetically favorable. However, as the magnetic field at the sample edges approaches H_{c1} and vortices begin to nucleate, several energy barriers prevent their penetration into the bulk of the superconductor until the field at the edge is increased to the penetration field H_p, where $H_p > H_{c1}$.[1,2] An additional complication is the existence of large demagnetization factors, dependent on sample size and shape, which enhance the local field at the sample edges and reduce the value of the applied field where first penetration occurs. These enhancement factors can be very difficult to estimate accurately for general sample shapes. The possible penetration of flux inside a superconducting sample and the associated resistive losses experienced when a current is applied represent serious problems for applications of superconductivity. Hence it is vital to develop a complete understanding of surface barriers and more accurate models of demagnetization effects in various sample geometries to be able to extend the range of the flux-free state.

II. EXPERIMENTAL METHOD

Microfabricated structures on the surface of $Bi_2Sr_2CaCu_2O_{8+\delta}$ (BSCCO) single crystals have been shown to be model systems for investigating surface barriers (Bean-Livingston and geometrical) to flux penetration.[3,4] Previous works have focused on investigations of the temperature dependence of penetration into circular disks of various sizes. Here we describe an extension of these studies to look at the role that the sample geometry plays in the vortex penetration process. We have fabricated arrays of BSCCO disks, pentagons, squares, and triangles of fixed known area and measured their temperature-dependent penetration fields $H_p(T)$ using differential magneto-optic imaging (MOI). In the regime studied $H_p(T)$ was observed to decay exponentially with temperature and, in stark conflict with conventional estimates of the demagnetization factors, *falls* with the decreasing degree of symmetry of the sample.

Single crystals of BSCCO ($T_c \approx 92K$) were grown using the floating zone method.[5] Arrays of shallow pillars with the four different symmetries were etched into the surface of freshly cleaved crystals using optical lithography and argon ion-milling techniques. Optical micrographs of typical sample arrays are shown in Fig. 1. In each case, structures of different area are patterned at the corners of a repeating 40 μm square cell and the pillar height is 300 nm. The four sizes of the circular disks (A1-A4) have diameters: 20, 15, 10 and 5 μm and the dimensions of the other regular polygons have been designed to conserve these four areas (c.f., Table I).

We assume that the influence of the underlying optimally doped BSCCO platelet on $H_p(T)$ is negligible due to the substantial suppression of bulk pinning in our measurement temperature range (45 K – 80 K).

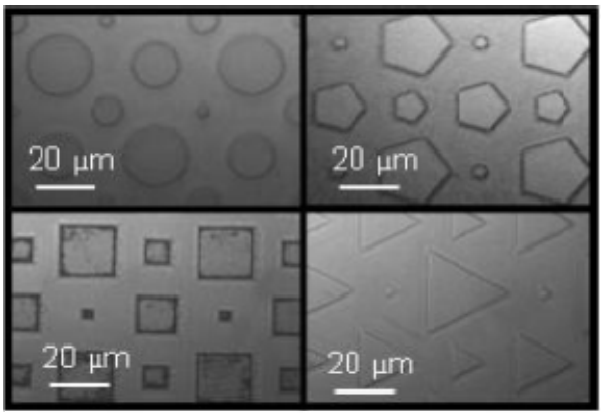

Fig 1. Optical micrographs of four typical BSCCO samples.

Mesostructure	Area (μm^2)
A1	$\pi \times 10^2 = 314.2$
A2	$\pi \times 7.5^2 = 176.7$
A3	$\pi \times 5^2 = 78.5$
A4	$\pi \times 2.5^2 = 19.6$

TABLE I. Areas of the four structure sizes labelled A1-A4, equivalent to disks of diameter 20, 15, 10 and 5 μm respectively.

Magneto-optical imaging (MOI) has previously been shown to be a very useful technique for studying flux penetration into BSCCO mesostructures.[3] A schematic of the experimental setup is shown in Fig 2. The technique exploits the magneto-optic Faraday effect: the rotation of the plane of polarization of light in the presence of a magnetic field. Key to the emergence of MOI as a tool for detecting stray fields on mesoscopic superconductors was the development of ferrimagnetic garnet films with in-plane anisotropy, which greatly enhance the sensitivity of the system.[6] In this instance, a Bi-doped yttrium iron garnet film was pressed into intimate contact with the sample using screws. The whole assembly was then attached to the cold head of a cryocooler for imaging experiments. Further details of the garnet and the entire measurement system can be found in the literature.[7]

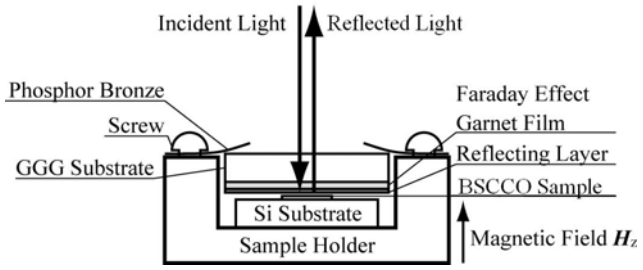

Fig 2. Schematic diagram of the experimental magneto-optical imaging setup.

The numerical difference between two images captured at slightly different magnetic fields (henceforth termed a difference image) is used to map flux penetration, as the subtraction enhances contrast and removes unwanted artifacts, such as domain walls and scratches in the garnet indicator, from individual images. Figure 3 shows some typical difference images used to establish H_p in circular disk-shaped samples at 55 K. At low fields flux was found to enter only the interstitial areas of the array as seen in Fig. 3(a). At higher fields the most noticeable flux changes are those within the pillars. H_p is identified as the lowest field at which penetration into a structure of given area is observed.

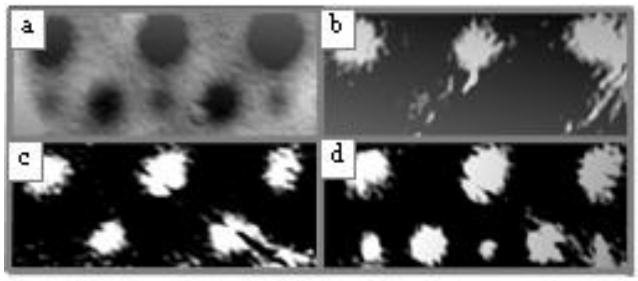

Fig 3. MO difference images of an array of disks at 55 K. Bright intensity marks areas of flux penetration. (a) [25 Oe – 0 Oe] displays the Meissner screening signature of the pillars as flux enters interstitial areas at low fields. (b) [35 Oe – 30 Oe], (c) [39 Oe - 34 Oe], and (d) [43 Oe -38 Oe] show flux entering the 20, 15 and 10 μm diameter shapes respectively as the field increases. The smallest (A4) structures lay outside the spatial resolution of this experiment.

III. EXPERIMENTAL RESULTS

Several experimental and theoretical studies have established the Bean-Livingston barrier as the dominant barrier for pancake vortices in BSCCO at $T > 15K$.[4, 8-10]. Theory predicts $H_p(T)$ will take the form:[4, 9]

$$H_p = P\frac{\sqrt{2}\kappa}{\ln\kappa}H_{c1}(0)\left[1-\left(\frac{T}{T_c}\right)^2\right]e^{-T/T_0}, \qquad (1)$$

where κ is the Ginzburg-Landau parameter, P is the inverse field enhancement factor and T_0 is a characteristic temperature for the penetration process. For ease of comparison with Eq. (1), Figs. 4 and 5 display experimental data in the form $\ln[H_p(T)/(1-(T/T_c)^2]$ versus T. Figure 4 displays penetration field data for the largest sized shape (A1) of each geometry in the temperature range 45 K – 75 K. Linear fits based on Eq. (1) have been plotted (choosing $T_0 = 34K$ and $T_c = 92K$), and are in excellent agreement with our data, confirming the exponential temperature dependence predicted by Eq. (1). The prefactors $[(P\sqrt{2}\kappa/\ln\kappa)H_{c1}(0)]$ extracted from these fits are discussed later, as they contain information regarding the surface field enhancement and quantify the trend that is clearly observed in Fig. 4: H_p falls systematically with decreasing sample symmetry for a given sample area.

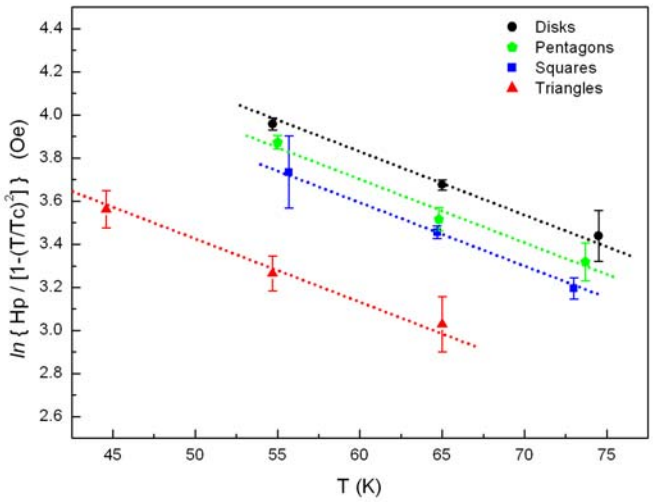

Fig 4. (Color online) $\ln[H_p(T)/(1-(T/T_c)^2]$ versus T for the largest BSCCO mesostructures (A1). Data points are experimental data; dashed lines are fits to Eq. (1) with $T_0 = 34K$ and $T_c = 92K$.

MOI spatial resolution is limited by the finite sample/garnet spacing, and accurate sample preparation was paramount in achieving high resolution. This, combined with cryocooler vibrations of the order of ~1μm made it impossible to resolve penetration of flux into the smallest A4 structures in all cases. A2 and A3 exhibit the same trend as the A1 structures shown in Fig. 4, with $T_0 = 34K$ again providing an excellent description using fits based on Eq. (1). To illustrate this point, Fig. 5 plots the temperature dependence of the penetration field for the three largest square structures, each of which is seen to exhibit the same exponential temperature dependence with a different size-dependent prefactor.

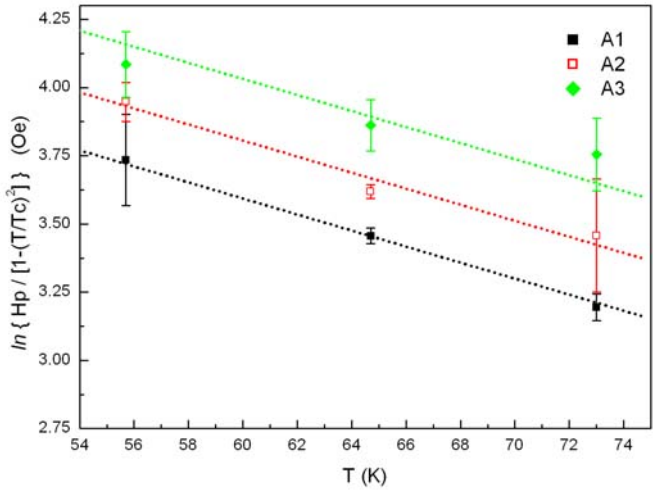

Fig 5. (Color online) $\ln[H_p(T)/(1-(T/T_c)^2]$ versus T for arrays of square BSCCO mesostructures. Data points are experimental data; dashed lines represent theoretical fits based on Eq. (1) with characteristic temperature $T_0 = 34K$ and $T_c = 92K$.

Analytical solutions for demagnetization factors exist only for ellipsoidal-shaped magnetic bodies. As a consequence, demagnetization effects in arbitrarily shaped superconducting bodies are commonly approximated by those for "equivalent" ellipsoids. For an ellipsoid with a magnetic field H_a applied parallel to one of the principal axes, the effective magnetic field (H_{eff}) at the equator is[11]

$$H_{eff} = \frac{H_a}{1-D}, \qquad (2)$$

where D is the demagnetisation factor which can take values between 0 and 1, and the inverse enhancement factor in Eq. (1) is $P = (1-D)$. For an oblate ellipsoid with principal axes (a, a, c) along (x, y, z) directions and with the field applied along z it can be shown that[11]

$$D = \frac{1}{e^3}\left(e - \sqrt{1-e^2}\,\sin^{-1} e\right), \qquad (3)$$

where $e = (1-c^2/a^2)^{1/2}$. Expanding (3) to second order in c/a yields

$$P = (1-D) \cong \frac{\pi}{2}\frac{c}{a} - 2\frac{c^2}{a^2}. \qquad (4)$$

One might expect that a good approximation to the field at the edge of a disk of radius R and thickness $d << R$ in a perpendicular field H_a could be obtained by replacing the disk by an oblate ellipsoid with major axis $b = R$ and minor axis $c = d/2$. Combining (2) and (4) (ignoring the second-order term) would yield the result for the field at the edge $H_{eff} = H_a(2a/\pi c) = H_a(4R/\pi d) \approx H_a(R/d)$. However, Geshkenbein and Larkin[12] suggested that a better approximation corresponds to a different choice of elliptical cross section with a larger semi-minor axis, such that the radius of curvature at the edge is approximately $d/2$.[12] (The radius of curvature of an oblate ellipsoid at $(x, y, z) = (a, 0, 0)$ is $\rho(a, 0, 0) = c^2/a$.) Zeldov *et al.*[13] have demonstrated that this leads to a more accurate value of $H_{eff} \cong H_a(R/d)^{1/2}$ in the limit $\lambda < d << R$, a result which was confirmed by experiments on mesoscopic BSCCO structures[3-4] and our own observations here. The same approach has been used to estimate the penetration field in long strips and disks.[14-15] Figure 6 shows the applied field at penetration plotted against the inverse quarter power of the sample area, $A^{-1/4}$. Since the areas (A1-A3) are proportional to the radius of the equivalent disks squared, the good linear fits are consistent with the expected functional relationship of $H_p \propto R^{-1/2}$. A more critical analysis of Fig. 6 reveals that, while the data for the triangular samples extrapolates to a point near the

origin for $A^{-1/4} = 0$ as expected from Eq. (1), the data for squares and disks extrapolate to significant positive intercepts (9 Oe and 17 Oe respectively). Since penetration must surely occur at H~0 for an infinite platelet this suggests that these data points in Fig. 6 would be better described by a sublinear relationship that passes close to the origin. This apparent discrepancy may be due to the fact that we are not strongly in the limit described in reference 13 since $d \sim \lambda$ in our samples. It is interesting to note that plots of similar data for somewhat thicker BSCCO disks and squares in reference 4 actually exhibit negative intercepts at $(d/R)^{1/2} = 0$.[4]

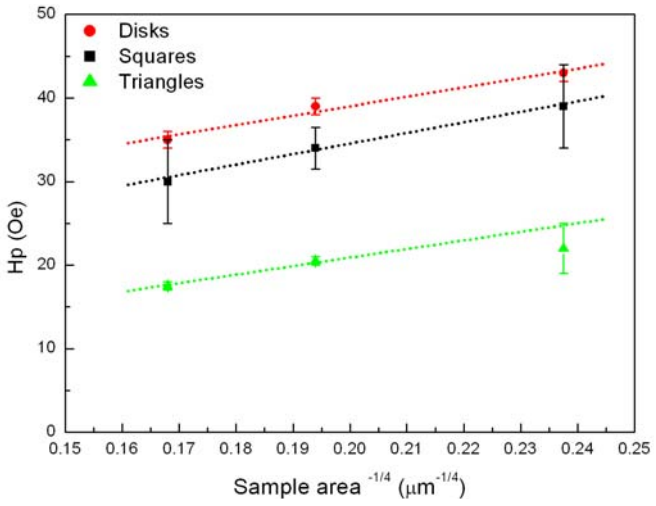

Fig 6. (Color online) H_p versus $A^{-1/4}$ for disk-shaped, square, and triangular BSCCO mesostructures at $T = 55K$. The smallest structures (A4) and the A3 pentagons were beyond the resolution of this experiment.

Theoretical fits to our experimental measurements based on Eq. (1) using $T_0 = 34K$ yield the values for the prefactor $[(P\sqrt{2}\kappa/\ln\kappa)H_{c1}(0)]$ recorded in Table II. These are in reasonably good agreement with other similar measurements in the literature.[3-4] Taking $\kappa \approx 100$ and $H_{c1}(0) \approx 100\ Oe$,[3,16] we can then estimate the values for the inverse enhancement factor P for each geometry and size.

The demagnetization factors of polyhedra have commonly been approximated by *inscribed* ellipsoids of revolution.[17] In our case, and imposing the above condition on the radius of curvature at the edge, $c^2/a = d/2$, this corresponds to a choice of $a = b = r_n$, $c = (r_n d/2)^{1/2}$ and (from Eqn. 4) $P_i(n) \cong (\pi^2 d/8r_n)^{1/2}$, where r_n is the inscribed radius of a regular polygon with n-fold rotational symmetry (the subscript i denotes use of an inscribed circle). However, noting that the radii of inscribed circles r_n vary as $r_3(tri) < r_4(squ) < r_5(pent) < r_\infty(disk)$, it is clear that this approach gives $H_{p3}(tri) > H_{p4}(squ) > H_{p5}(pent) > H_{p\infty}(disk)$. The experimentally measured field enhancement parameters (P_{exp}) are listed alongside these theoretical estimates (P_i) in Table II and it is clear that the trend of the predictions for inscribed ellipsoids are in direct contradiction with our experimental observations. We note that the penetration fields of similar freestanding BSCCO microstructures (circular disks and squares) were also compared in Ref. 4. Although the authors did not comment on it in that paper, and data were not presented at directly comparable temperatures for the two shapes, their penetration fields for squares also appear to be significantly lower than circular disks of the same width and thickness for $T \geq 45K$.

IV. DISCUSSION

Many theoretical studies have been devoted to the calculation of demagnetization factors for magnetic bodies with a range of regular shapes. Much of this work has arisen in the context of ferromagnetism where accurate demagnetization factors are vital for the precise calculation of magnetostatic energies. Since demagnetizing fields are not uniform in arbitrarily shaped bodies, such calculations yield effective average values; for example, the magnetometric demagnetizing factor of an arbitrary sample in the z-direction, D_z, can be defined as the factor that makes the magnetostatic self-energy per unit volume equal to $2\pi D_z M_s^2$, where M_s is its saturation magnetization. A comparison with estimates based on values obtained from equivalent ellipsoids is frequently made. For example, Aharoni presents analytical results for the demagnetization factors of rectangular ferromagnetic prisms and notes very significant discrepancies from values obtained for a prolate spheroid with the same aspect ratio.[18] To address this issue, Beleggia *et al.*[19] have calculated the equivalent ellipsoid for uniformly magnetized disks, cylinders with elliptical cross-section and prisms, by imposing equality between the demagnetization factors of the two shapes of *equal* volume. Demagnetization factors have also been calculated for magnetic materials under other assumptions, e.g., for a fixed value of the magnetic susceptibility, χ. Making an explicit connection to the Meissner state in superconductors, Pardo *et al.*[20] and Chen *et al.*[21] have numerically calculated the magnetometric demagnetization factors for perfectly diamagnetic ($\chi = -1$) square prisms and cylinders. In practice, however, penetration in our pillars occurs at the point on the surface where the effective field (demagnetizing field) is highest, and these *average* calculations are of little practical use. Moreover, none of these works accounts for the penetration of flux lines in a realistic way; for example, the field lines at the edges do not have the expected curvature as discussed above.[12]

Berdiyorov *et al.*[22] describe a theoretical study that addresses a situation much closer to the one found in our experiments. They have calculated numerical solutions to the non-linear Ginzburg-Landau equations for vortex penetration into mesoscopic superconducting disks, rings, and squares. They find that the Bean-Livingston energy barrier that has to be overcome for a single vortex to enter a sample is lower at the middle of one edge of a square

than on the circumference of a disk of the same width and thickness. Hence first flux penetration occurs at significantly lower fields in the square, in apparent agreement with our experimental observations. We note, however, that these calculations have been made for samples with $r = 4\xi$, $d = 0.1\xi$, and $\kappa = 1$ and so are in a very different regime from our samples with $r >> \xi$, $d >> \xi$, and $\kappa \approx 100$.

Finally we make the empirical observation that the qualitative trend exhibited by our experimental data is captured if we base equivalent ellipsoids on the radius of the *circumscribed* circle instead of the *inscribed* circle considered above. The radius, R_n, of a circumscribed circle surrounding an n-sided regular polygon with side of length S_n is

$$R_n = \frac{S_n}{2\sin(\pi/n)}. \qquad (5)$$

Choosing $a = b = R_n$, and $c = (R_n d/2)^{1/2}$, theoretical values of $P_c(n)$ (the subscript c denotes use of a circumscribed circle) for our BSCCO platelets have been generated by combining Eqs. (4) and (5) and are displayed in Table II. Comparing experimental data with the circumscribed circle model, we note that the trend with decreasing degree of symmetry is now correct. However, a comparison of columns $P_{\exp}/P_{ref}$ and $P_c(n)/P_{c,ref}$, where the inverse enhancement factors have been normalized by that of a reference disk of area A1, reveals that the theoretical predictions do consistently overestimate the observed values. Aside from these numerical differences, we believe that this is the first time that it has been pointed out that equivalent ellipsoids based on ***circumscribed*** rather than ***inscribed*** circles yield a qualitatively better estimate of the trend in demagnetization factors as a function of degree of symmetry in polygon-shaped superconducting platelets. Our observations have rather important implications for the estimation of appropriate effective demagnetization factors for flux penetration into arbitrarily shaped superconducting bodies. In particular, it is surprising that the experimental field enhancement factor for the triangular platelets is so much larger than the other structures. Clearly a model based on circumscribed circles is too simple to capture all the physics of the probelm of flux penetration which must also consider the disribution of supercurrent densities and the role of sharp/rounded corners etc. Hence we hope that this paper will stimulate new theoretical work to fully understand this.

This work was supported by EPSRC-U.K. Grant No. EP/E039944/1, the Royal Society International Joint Project No. 2006/R3 and by JSPS Bilateral Joint Research Projects between Japan and U.K. Our work at the Ames Laboratory was supported by the Department of Energy - Basic Energy Sciences under Contract No. DE-AC02-07CH11358.

Mesoscopic Structure		Prefactor (Oe)	$P_{\exp}$	$P_{\exp}/P_{\mathrm{ref}}$	$P_{\mathrm{i}}(\mathrm{n})$	$P_{\mathrm{i}}(\mathrm{n})/P_{\mathrm{i,ref}}$	$P_{\mathrm{c}}(\mathrm{n})$	$P_{\mathrm{c}}(\mathrm{n})/P_{\mathrm{c,ref}}$
A1	- Disk	270 ± 5	0.0893 ± 0.0016	1.000	0.166	1.000	0.166	1.000
	- Pentagon	236 ± 5	0.0787 ± 0.0018	0.882	0.172	1.032	0.157	0.942
	- Square	211 ± 3	0.0699 ± 0.0010	0.783	0.175	1.054	0.151	0.907
	- Triangle	134 ± 3	0.0446 ± 0.0010	0.500	0.185	1.112	0.137	0.823
A2	- Disk	306 ± 15	0.1053 ± 0.0053	1.179	0.188	1.131	0.188	1.131
	- Square	262 ± 7	0.0877 ± 0.0022	0.983	0.198	1.189	0.171	1.027
A3	- Square	329 ± 18	0.1136 ± 0.0061	1.273	0.233	1.402	0.202	1.217

TABLE II. Experimentally and theoretically derived inverse enhancement factors *P* for various BSCCO mesostructures. The areas of the n-sided regular polyhedra A1-A3 are contained in Table I. $P_{\mathrm{i}}(\mathrm{n})$ and $P_{\mathrm{c}}(\mathrm{n})$ are theoretically derived using the methods of inscribed and circumscribed ellipsoids respectively. P_{ref}, $P_{\mathrm{i,ref}}$ and $P_{\mathrm{c,ref}}$ are the experimental and theoretical values of *P* for the A1 disk structure. The height of mesoscopic pillars is 300 nm in all cases.

1 C. P. Bean and J. D. Livingston, Phys. Rev. Lett. **12**, 14 (1964).

2 E. Zeldov, A. I. Larkin, V. B. Geshkenbein, M. Konczykowski, D. Majer, B. Khaykovich, V. M. Vinokur, and H. Shtrikman, Phys. Rev. Lett. **73**, 1428 (1994).

3 M. R. Connolly, M. V. Milošević, S. J. Bending, and T. Tamegai, Phys. Rev. B **78**, 132501 (2008).

4 Y. M. Wang, A. Zettl, S. Ooi, and T. Tamegai, Phys. Rev. B **65**, 184506 (2002).

5 S. Ooi, T. Shibauchi, and T. Tamegai, Physica C **302**, 339 (1998).

6 C. Jooss, J. Albrecht, H. Kuhn, S. Leonhardt, and H. Kronmuller, Rep. Prog. Phys. **65**, 651 (2002).

7 T. Tamegai, M. Matsui, M. Yasugaki, Y. Tokunaga, and M. Tokunaga, NATO Science Series B: Physics Vol. 142 (Kluwer, Dordrecht, 2004) (2004).

8 M. S. James, S. T. Stoddart, S. J. Bending, S. Aukkaravittayapun, P. J. King, and M. Henini, Phys. Rev. B **56**, R5771 (1997).

9 L. Burlachkov, V. B. Geshkenbein, A. E. Koshelev, A. I. Larkin, and V. M. Vinokur, Phys. Rev. B **50**, 16770 (1994).

[10] R. A. Doyle, S. F. W. R. Rycroft, C. D. Dewhurst, E. Zeldov, I. Tsabba, S. Reich, T. B. Doyle, T. Tamegai, and S. Ooi, Physica C **308**, 123 (1998).
[11] E. A. Lynton, *Superconductivity* (Methuen, London, 1962).
[12] V. B. Geshkenbein and A. I. Larkin (private communication).
[13] E. Zeldov, J. R. Clem, M. McElfresh, and M. Darwin, Phys. Rev. B **49**, 9802 (1994).
[14] M. Benkraouda and J. R. Clem, Phys. Rev. B **53**, 5716 (1996).
[15] J. R. Clem and A. Sanchez, Phys. Rev. B **50**, 9355 (1994).
[16] L. Burlachkov, Phys. Rev. B **47**, 8056 (1993).
[17] D. J. Craik, Brit. J. Appl. Phys. **18** 1355 (1967).
[18] A. Aharoni, J. Appl. Phys. **83**, 3432 (1998).
[19] M. Beleggia, M. De Graef, and Y. T. Millev, J. Phys. D-Appl. Phys. **39**, 891 (2006).
[20] E. Pardo, D. X. Chen, and A. Sanchez, J. Appl. Phys. **96**, 5365 (2004).
[21] D. X. Chen, E. Pardo, and A. Sanchez, J. Magn. Magn. Mater. **306**, 135 (2006).
[22] G. R. Berdiyorov, L. R. E. Cabral, and F. M. Peeters, J. Math. Phys. **46** (2005).